

www.acsanm.org Article

Atomic-Layer Deposition of the Single-Atom Pt Catalyst on Vertical Graphene for H₂ Sensing

Bo Liu,* Zhaojun Han, Avi Bendavid, Philip J. Martin, Priyank V. Kumar, Yousof Haghshenas, Mohammed Alamri, and Judy Z. Wu*



Cite This: ACS Appl. Nano Mater. 2024, 7, 22605-22616



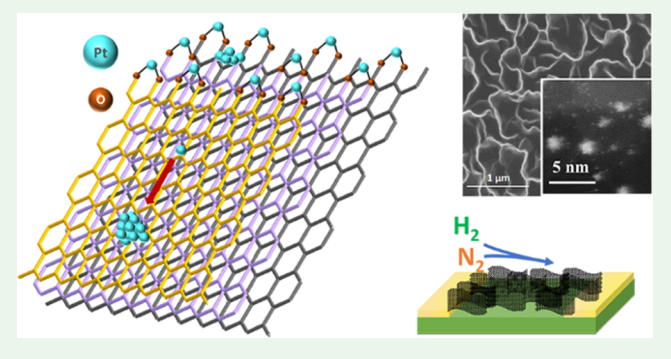
ACCESS

III Metrics & More

Article Recommendations

s Supporting Information

ABSTRACT: Single-atom catalysts have the advantage of high chemical efficiency, which requires atomic-scale control during catalyst formation. In order to address this challenge, this work explores the synthesis of single-atom platinum (SA-Pt) catalysts using atomic-layer deposition (ALD) on vertical graphene (VG), in which a large number of graphene edges serve as energetically favorable nucleation sites for SA-Pt, as predicted by density functional theory calculations. Interestingly, SA-Pt has been achieved on VGs at low ALD cycle numbers of up to 60. With a further increase in the number of ALD cycles, an increasing number of Pt clusters with diameters <2 nm and Pt nanoparticles (NPs) with diameters >2 nm become dominant (nano-Pt @VG). This is



in contrast to the observation of predominantly nano-Pt on other carbon nanostructures, such as carbon nanotubes and monolayer graphene, under the same ALD growth conditions, indicating that the edge states on VG indeed play a critical role in facilitating the formation of SA-Pt. Profound differences are revealed in a comparative study on H_2 sensing. SA-Pt exhibits both a higher sensitivity and faster response than its nano-Pt counterpart by more than an order of magnitude, illustrating the high catalytic efficiency of SA-Pt and its potential for gas sensing and a variety of other catalytic applications.

KEYWORDS: single-atom catalyst, vertical graphene, atomic-layer deposition, platinum, hydrogen sensor

1. INTRODUCTION

Noble metals have been shown to play a critical role as catalysts to boost surface chemical reactions in many important processes, including the dissociation of target gas molecules, adsorption of oxygen species in air, and other relevant chemical and electrochemical processes, and can thus be utilized in a large variety of industrial applications, including food, energy, and environment.^{1,2} Various metal catalytic nanostructures have been investigated by taking advantage of the large surfaceto-volume ratio that increases monotonically with decreasing dimensions of the nanostructures.^{3,4} For example, a sensor decorated with noble metal catalysts, the template (or electrode) material, and morphology play a critical role in determining the catalyst's morphology, concentration, and effective interface with the electrode, which in turn affects the device sensitivity. In gas sensors, the template needs to possess not only a high sensing surface area that allows efficient charge transfer for high sensitivity and sensing speed but also a compatible surface mechanism to enable anchoring and formation of the desired morphology for the deposited catalyst. Carbon-based nanostructures such as carbon nanotubes (CNTs) and graphene are considered superior template candidates for gas sensors.^{6,7} During gas molecule sensing, the interactions of the adsorbed gas molecules on the surface of the carbon nanostructures perturb their electronic structures, causing charge doping of the carbon nanostructures, and hence, the template conductivity changes as output "signals" of the sensor.

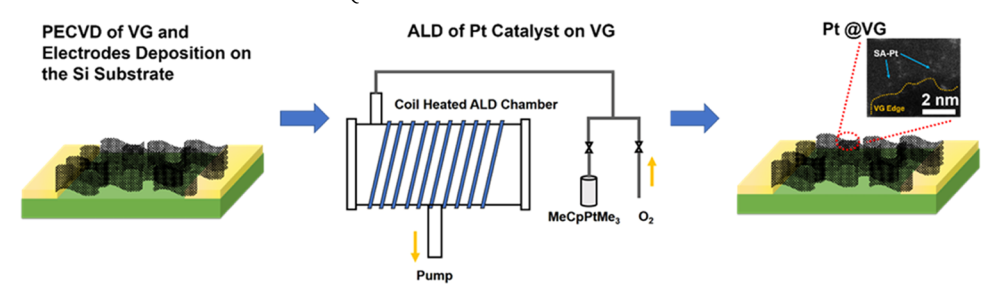
Among the many carbon nanostructures, single-wall carbon nanotubes (SWCNTs) and monolayer graphene are particularly attractive since all carbon atoms can be considered surface atoms capable of absorbing gas molecules. They show low electronic noise due to their high-quality crystal lattice and, hence, are capable of screening small amounts of charge fluctuations. However, the gas sensors based on these two templates have limited sensitivity due to the issues of bundling of the SWCNTs template and the lack of an efficient sensing area in two-dimensional (2D) graphene. This has motivated the recent exploration of three-dimensional (3D) templates based on carbon nanostructures, and enhanced sensitivity has been reported. Examples include SWCNT films, SWCNT/

Received: June 14, 2024
Revised: September 9, 2024
Accepted: September 17, 2024
Published: October 1, 2024





Scheme 1. Schematic of Fabrication of ALD Pt @VG



graphene nanohybrids, and vertical graphene (VG). ^{6,13} Among these, VG emerges as a promising alternative to 2D graphene due to its unique porous structure complemented by the exceptional properties of 2D graphene, rendering it an attractive candidate for gas sensors and many other applications. Compared to 2D planar graphene, 3D VG provides a significantly higher surface area and highly porous volume for the catalyst nanoparticles and gas molecule adsorption. ^{14,15}

Considering that the maximum surface-to-volume ratio can be achieved on single-atom catalysts (SACs), exploration of approaches to generating atomic catalysts has recently emerged as an intensive research focus. $^{16-18}$ Due to their special coordination environment, metal atoms in the SAC have special electronic structures different from their metal nanoparticle and nanocluster counterparts consisting of hundreds or thousands of metal atoms. 16 Consequently, SAC may exhibit unique characteristics, including long-term stability, high selectivity, and repeatability. 19 Moreover, SAC is an effective way to reduce the overall cost of the catalyst while achieving comparable or higher performance, especially when it comes to expensive noble metal catalysts, such as Pt or Pd. Motivated by this, SAC has been extensively studied and investigated in several recently reported gas sensors. For example, Zeng et al. reported an atomically deposited Ag on a tungsten oxide nanoplate (AD-Ag-WO₃) sensor using a hydrothermal method, which showed an exceptionally high response to triethylamine (TEA) and low operating temperature owing to the advantage of Ag SAC.²⁰ Tian et al. studied atomically dispersed Co on a MgO template via a supportsacrificial approach and achieved high room temperature sensitivity to NH₃ and high stability.²¹ Therefore, achieving SAC is important for high sensitivity but requires precise control of the catalyst nucleation and growth with atomic precision. It is well known that the morphology and size of metal catalyst nanostructures are affected by the surface states of carbon nanostructures. In particular, defects on carbon nanostructures often serve as nucleation sites. 22-24 In most carbon nanostructures, defects occur in an uncontrollable manner, resulting in difficulties in controlling the morphology and size of metal catalysts, especially in achieving SAC. VG differs from most other carbon nanostructures in the presence of a large number of dangling bonds, especially at the exposed edges of VG, which could provide promising nucleation sites for SAC.²⁵ On the other hand, atomic precision is required to control the deposition of the metal catalyst in order to achieve SAC.

Among other approaches, atomic-layer deposition (ALD) provides unique advantages of the surface-functional group-directed precursor nucleation and well-defined ligand exchange of the unique self-limitation mechanism in growth, both of

which are critical to the achievement of SAC.²⁶⁻²⁸ This means that VG and ALD may provide a perfect combination for the exploration of SAC formation. Motivated by this, this work explores the ALD growth of a platinum single-atom catalyst (SA-Pt) on VG (Scheme 1); for the first time to our knowledge, SA-Pt has been achieved within an optimal ALD window on the VG platform, beyond which Pt clusters of diameters <2 nm and Pt nanoparticles (NPs) of diameters >2 nm (nano-Pt) become dominant. Density functional theory (DFT) simulations have revealed higher stability of SA-Pt near the edge states of VGs in contrast to the more stable nano-Pt. In order to elucidate the effect of the Pt catalyst morphology and dimensions, a comparative study of H2 sensing was conducted using two types of ALD Pt catalysts. A distinctive benefit of SA-Pt is its much faster response speed and higher sensitivity than those of its nano-Pt counterparts. DFT simulation of the Pt catalyst size effect revealed the lowering of the H₂ adsorption energy by SA-Pt from that of its nanoscale counterparts. Therefore, this result illustrates the importance of atomic-scale control of catalyst nucleation on the template and deposition to achieve metal SAC and sheds light on the role of SAC in sensing.

2. METHODS

2.1. Sample Fabrication. Scheme 1 illustrates the fabrication process of ALD Pt @ VG samples, which involves three major steps: synthesis of VG on the Si substrates, deposition of electrodes for H_2 sensor applications, and decoration of the Pt catalyst.

2.1.1. VG Template Synthesis on the Si Substrate. VG was synthesized using plasma-enhanced chemical vapor deposition (PECVD), as described in our previous studies. ^{29,30} Briefly, the Si substrate was first placed in a PECVD chamber, which was evacuated to less than 1.5×10^{-4} Torr. Ar flow was then introduced at 10 sccm into the chamber, and the pressure was adjusted to 1×10^{-2} Torr. A 13.56 MHz radio frequency (RF) plasma source was turned onto ignite the plasma at a power of 1000 W to pretreat the Si substrate for 10 min. Next, 10 sccm CH₄ and 10 sccm H₂ gas mixtures were introduced into the chamber to initiate the growth of VG. The VG sample was obtained after approximately 10 min of growth in PECVD.

2.1.2. Electrode Deposition on VG. A group of four Nb (40 nm)/Pd (10 nm) electrodes, each with a lateral dimension of 4 mm (length) \times 2 mm (width), was deposited on top of the VG samples through a shadow mask using magnetron sputtering. The separation distance between the neighboring electrodes was 0.3 mm, which defined the effective sensor channel length. Three channels were obtained for the same sample and were typically measured for consistency. The sputtering chamber was prepumped to a high vacuum of \sim 5 \times 10⁻⁷ Torr and then filled with high-purity Ar (99.999%) stabilized at a pressure of 14 mTorr at a flow rate of 2.5 sccm. The DC powers for sputtering Pd and Nb were set to 50 and 330 W, respectively. The use of Nb improves the adhesion of the Pd electrode to the substrate.

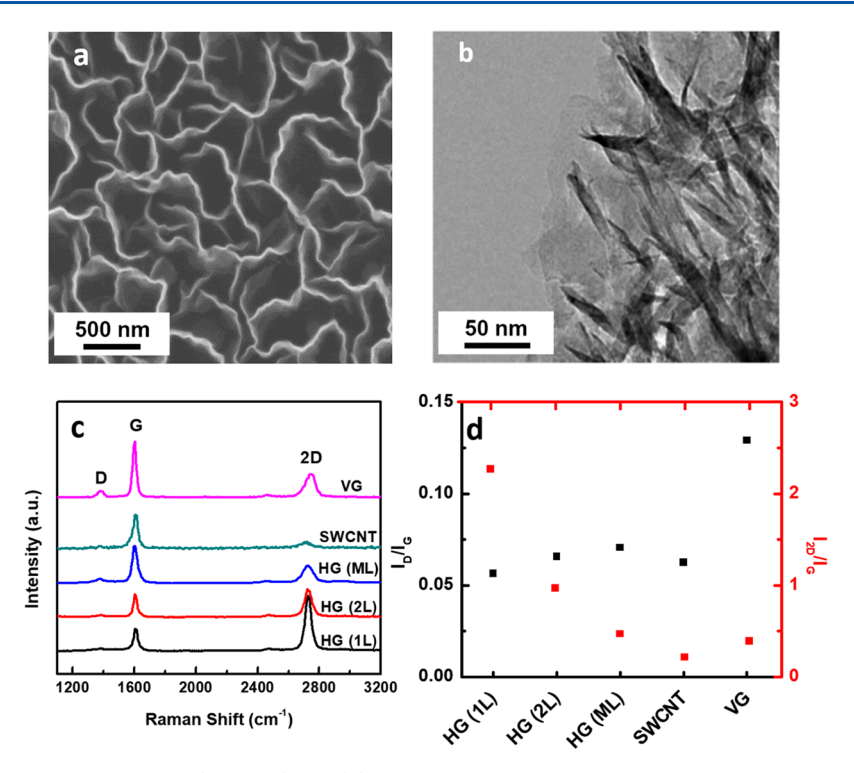


Figure 1. (a) Representative SEM image of VG (top view) and (b) TEM image of VG transferred onto a carbon-coated Cu mesh. (c) Comparison of the Raman spectra of VG (purple), SWCNT film (green), HG (1L) (black), bilayer (HG(2L)) (red), and HG(ML) (blue). (d) $I_{\rm D}/I_{\rm G}$ (black) and $I_{\rm 2D}/I_{\rm G}$ (red) ratios of the same five samples in (c).

2.1.3. Growth of Platinum Catalyst on VG with Electrodes. Pt catalyst growth was accomplished in an ALD chamber by alternating exposure to trimethyl(methylcyclopentadienyl)platinum(IV) (MeCpPtMe₃, Sigma-Aldrich) and oxygen pulses at 300 °C. ³¹ During the ALD growth, a constant flow (5 sccm) of ultrahigh-purity nitrogen (99.999%) carrier gas was passed through the reactor. The MeCpPtMe₃ precursor was heated to 60 °C to increase its vapor pressure. In one ALD deposition cycle (c), reactant exposure lasted 3 s for the MeCpPtMe₃ pulse and 1 s for the oxygen pulse, each followed by a high-purity nitrogen (99.999%) purge of 60 s. A Pt catalyst was deposited on the VG samples using ALD with a selected number of ALD cycles (20, 40, 60, and 80 c) for controlling the amount of Pt coated on the VG templates. Reference samples of Pt-decorated SWCNT/graphene templates were fabricated under the same ALD conditions.

2.2. Characterization of the Sample Microstructure. 2.2.1. High-Resolution Scanning Transmission Electron Microscopy. High-resolution scanning transmission electron microscopy (HRSTEM) was performed using a JEOL JEM-F200 microscope. The Pt @VG sample was removed from the Si substrate and dispersed in an ethanol solution before being drop-casted on a holey carbon copper TEM mesh. Scanning electron microscopy (SEM) images of the SWCNT sample with 20 c of ALD Pt coating were taken using a Hitachi SU8230 ultrahigh-resolution scanning electron microscope.

2.2.2. Raman Spectroscopy. The Raman spectra of the carbon nanostructure templates, including VG and monolayer, bilayer, and multilayer horizontal graphene, were measured using a WiTec Alpha300 confocal micro-Raman system equipped with a piezoelectric sample stage (maps of Raman bands confirm sample uniformity) with a 488 nm excitation laser (power ~30 mW and integration time of 1 s).

2.3. Characterization of H_2 Sensing. The H_2 response and sensitivity were measured using Pt @VG sensors in a vacuum chamber under a mixed H_2/N_2 gas flow. The Pt @VG sensors were mounted on a sample stage inside the chamber with an electric feed-through for the electric connection of the sample to external electronics. Before the measurement, the chamber was purged with N_2 flow for about an hour to remove residual gas molecules. The

concentration of H_2 was controlled by controlling the flow ratio of H_2 and N_2 gases using an MKS four-channel flow rate controller (MKS 946). For example, in order to obtain a 10% H_2 concentration, the H_2/N_2 ratio was set to 20 sccm (H_2):180 sccm (N_2). In this work, the concentration of H_2 was varied in the range of 1–30%. Current—time (I-t) curves were recorded on the Pt @VG sensors at a constant bias voltage (V) using a CHI Instrument CHI660D electrochemical workstation in response to H_2 flow on and off in a vacuum chamber. The I-t curves were later converted to resistance—time (R-t) curves using Ohm's law R = V/I, where V was set to 0.1 V in this work for responsivity calculation. The resistance of the connection between the CHI660D electrochemical workstation and device was measured to be 0.5–0.8 Ω , which is negligible compared to the resistance of VG-based H_2 sensor of 50–100 Ω and is important to obtaining a high signal-to-noise ratio, typically in the range 100:1 or better.

2.4. DFT Simulation. DFT calculations were conducted using the plane-wave Vienna Ab initio Simulation Package (VASP) code. 32,33 The core electrons were treated using the projector augmented wave (PAW) method 34 and the Perdew–Burke–Ernzerhof (PBE) exchange-correlation functional was employed. 35 The wave functions were expanded with a kinetic energy cutoff of 500 eV and a γ -point k-grid was used. All relaxations were performed until the residual forces on the atoms were less than 0.1 eV/Å. A vacuum region of >10 Å was maintained along the axis perpendicular to the surface to prevent interactions between the periodic images.

An SWCNT comprising 120 carbon atoms, characterized by dimensions of (5, 5) and a length of 11.79 Å, was carefully fabricated using the atomic simulation environment (ASE) Python package.³⁶ The initial structure of graphene, composed of 72 carbon atoms arranged within a single plane (monolayer), was similarly established utilizing the ASE suite. Meanwhile, a Pt cluster, composed of 13 Pt atoms structured in an octahedral geometry (O_h), was systematically generated employing the ASE toolkit. To find the most stable adsorption configuration of hydrogen atoms on the graphene and Pt cluster surfaces, three different adsorption configurations were considered, and the one with the lowest energy was assumed to be the most stable configuration.

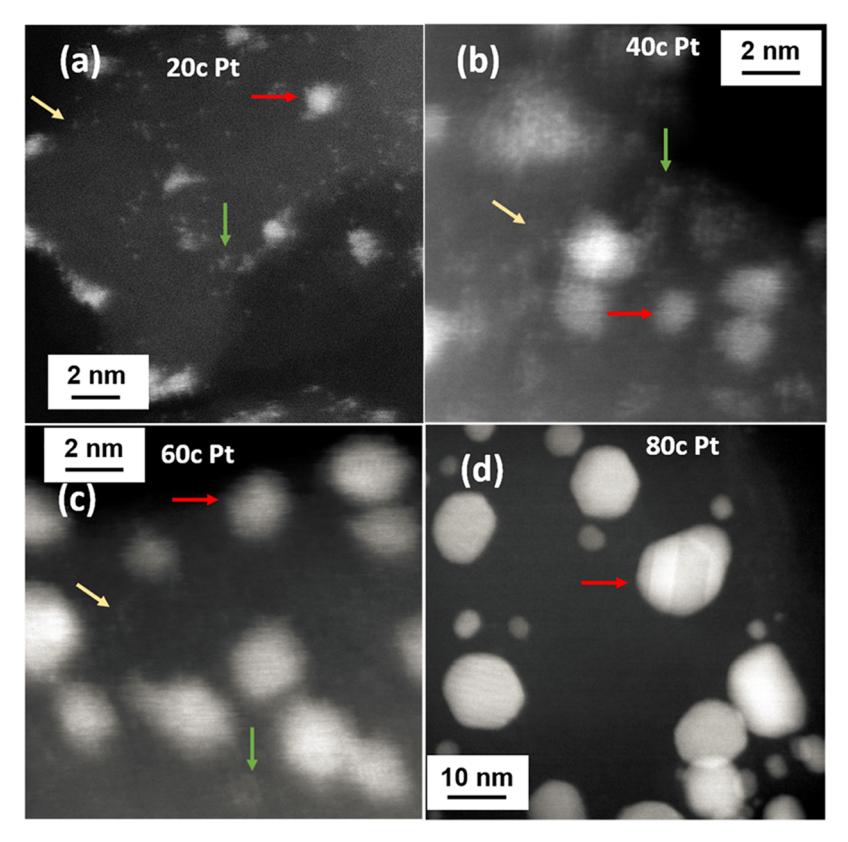


Figure 2. HRSTEM images of Pt @VG with different Pt ALD cycles: (a) 20 c, (b) 40 c, (c) 60 c, and (d) 80 c, respectively. Yellow, green, and red arrows indicate SA-Pt, Pt clusters (diameter < 2 nm), and Pt nanoparticles (diameter > 2 nm), respectively.

The adsorption energies were calculated using eq 1

$$E_{\rm ads} = E_{\rm product} - E_{\rm reactant} \tag{1}$$

3. RESULTS AND DISCUSSION

The 3D morphology of VG is revealed in the SEM image shown in Figure 1a with massive vertical walls of graphene. The wall thickness of VG was measured to be approximately 1-5 nm, indicating that the VG walls consisted of several layers of graphene sheets. The cavities formed by the surrounding VG walls range from hundreds of nanometers to a few micrometers in size, suggesting a macroscopically porous structure in VG that allows efficient access to molecules (gas, chemicals, etc.). The effective surface area of the porous VG sample was estimated to be ~400 m² g⁻¹ in our previous work.³⁷ This large surface area of VG enables sufficient adsorption-desorption of molecules on the VG walls, making the VG nanostructure an excellent candidate as a 3D template for sensors. Figure 1b shows a representative TEM image of VG grown on the Si substrate that was transferred onto a carbon-coated Cu mesh for TEM. Stacking of multiple highquality graphene sheets in the VG sample can be clearly observed. Figure S1 exhibits an SEM image of VG removed from the SiO₂/Si substrates after CVD growth. Multiple layers of VG can be clearly seen, with a layer height of around ~3.46 μm.

Figure 1c compares the Raman spectra of VG and 2D horizontal graphene (HG) of the monolayer, bilayer, and multilayer. For convenience, they are denoted as HG (1L), HG (2L), and HG (ML). The two predominant peaks located at 1602 and 2754 cm⁻¹ correspond to the G and 2D peaks of graphene, respectively. These peaks are associated with the

doubly degenerate zone center $E_{\rm g}^{\ 2}$ mode and the second order of zone-boundary phonons.³⁸ The D peak that appears at around 1380 cm⁻¹ is related to the breathing modes of sp² carbon atoms in rings with defects or disorders and could be used to quantitatively assess the presence of defects. In addition, the Raman spectrum of the SWCNT film is also shown in Figure 1c, which has D, G, and 2D peaks at the same location as HG and VG. Figure 1d shows the calculated 2D/G intensity ratio $(I_{2D}/I_{G}, \text{ black})$ and D/G intensity ratio $(I_{D}/I_{G}, I_{G})$ red) values from Figure 1c for the four aforementioned samples. As anticipated, the $I_{\rm 2D}/I_{\rm G}$ ratio decreases monotonically with the number of graphene layers. Specifically, the $I_{\rm 2D}/$ $I_{\rm G}$ ratios for HG (1L), HG (2L), HG (ML), and SWCNT in Figure 1d are 2.268, 0.968, and 0.469, respectively, which are consistent with the reported values for the corresponding HG and SWCNT samples. 39,40 The SWCNT sample shows an I_{2D} / $I_{\rm G}$ value of 0.213, demonstrating its more semiconductor behavior than metallic.⁴¹ The VG sample has an I_{2D}/I_{G} value of 0.390, confirming its multilayer nature as revealed in the TEM studies (Figure 1a,b). Interestingly, the three HG and SWCNT samples have comparable and low I_D/I_G ratios of around 0.055-0.065, indicating that the defect concentrations in these samples are fairly low. This is in contrast to the more than twice the $I_{\rm D}/I_{\rm G}$ ratio of the VG sample, as shown in Figure 1d, indicative of more defect sites with abundant edges on VG that are desired for the anchoring of SA-Pt during the ALD of the

The HRSTEM images of the Pt @VG samples with 4 different numbers of ALD cycles (or "c") of 20, 40, 60, and 80 c are compared in Figure 2a-d, respectively. In the samples with fewer ALD cycles up to 60 c, distinctively different Pt structures can be seen on the Pt @VG samples, including SA-

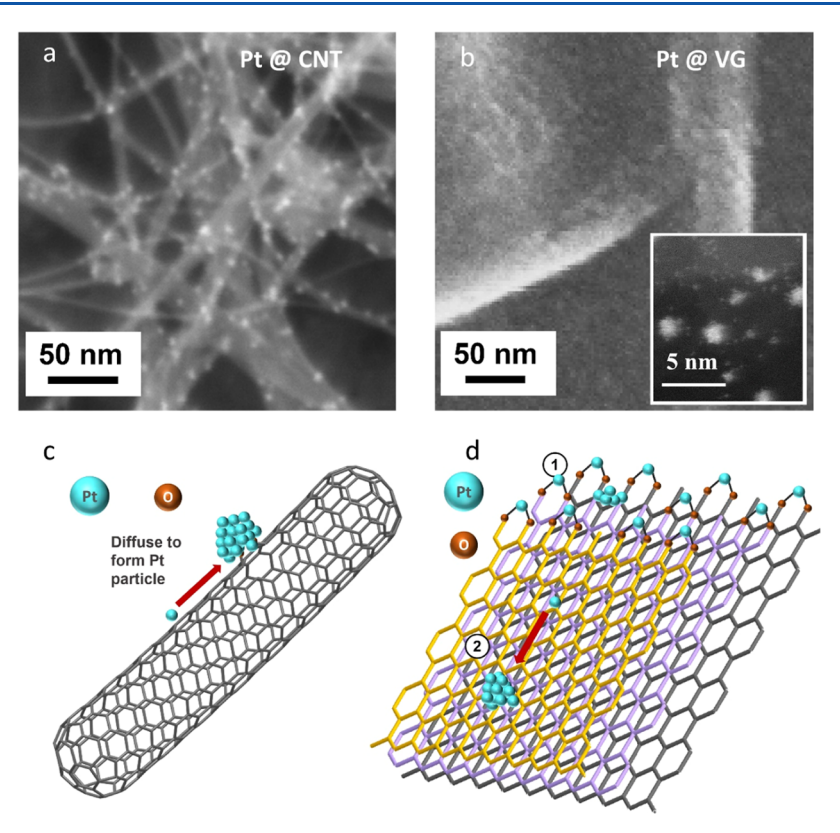


Figure 3. (a) SEM image of 20 c Pt @SWCNT; (b) SEM image of 20 c Pt @VG, where the inset shows the HRSTEM zoom-in image; (c) proposed nano-Pt growth mechanism on SWCNT through diffusion of Pt atoms to sparse nucleation sites (defects) on the SWCNT; and (d) proposed growth mechanisms of Pt SAC via nucleation on the VG edge states and nano-Pt on the basal plane of VG through diffusion of Pt atoms to sparse nucleation sites (defects) on VG.

Pt (yellow arrows) and nano-Pt of small Pt clusters of dimensions <2 nm (green arrows) and crystalline Pt NPs of dimensions >2 nm (red arrows). Interestingly, the proportions of the three types of Pt structures vary with the number of ALD cycles or the amount of Pt decorated on VG. Specifically, the proportions of the first two types (SA-Pt and nano-Pt) decrease with the increasing ALD cycle number while the last one (Pt clusters) exhibits the opposite trend. In the Pt @VG with the least ALD cycle number of 20 c (Figure 2a), the majority of the decorated Pt is SA-Pt, while a small portion of Pt clusters and Pt NPs of small dimensions coexist. In the 40 c sample (Figure 2b), in which twice the amount of Pt is expected to be decorated on VG, the proportion of nano-Pt becomes larger than that in the case of Pt @VG with 20 c ALD Pt. In the Pt @VG sample with 60 c ALD Pt (Figure 2c), the concentration and size of the nano-Pt are further increased compared to those observed in the Pt @VG samples with 20 and 40 c Pt. In the VG sample with 80 c ALD Pt (Figure 2d), SA-Pt and clusters are barely observable. Instead, large Pt NPs with increased concentrations are relatively polydisperse in size, ranging from a few nanometers to $\sim\!20$ nm. The Pt NPs were confirmed to be highly crystalline, as illustrated by the appearance of facets on the NPs. Figure S2 summarizes the percentage histogram of the ALD Pt forms (SA, cluster (diameter < 2 nm), and NP (diameter > 2 nm)) as a function of the number of ALD cycles. Overall, as the number of ALD cycles increases, the percentage of SA-Pt decreases while that of nano-Pt increases. For VG with 20, 40, 60, and 80 c ALD Pt, the SA proportions are 83.1, 45.8, 36.4, and 0%, respectively. The trend in the variation of the Pt structure morphologies, dimensions, and concentrations revealed the important role of VG in facilitating the nucleation of Pt from the Pt ALD precursor. In particular, a large amount of SA-Pt in Pt @VG with lower ALD cycle numbers confirms that the initial Pt structure is predominantly in the atomic form. This observation is important because it confirms that the combination of VG and ALD indeed provides a viable scheme to achieve SA-Pt by controlling the nucleation sites and growth mechanisms. When an additional amount of Pt was introduced by increasing the ALD cycle number or Pt amount, further growth from SA-Pt to nano-Pt led to both increased concentrations and sizes of the two types.

Figures 3a,b compare the morphologies of the Pt structures grown on SWCNTs and VG with 20 c ALD Pt under the same ALD growth conditions. The very different morphologies of the Pt structures on the two types of templates again demonstrate the critical role of VG in the nucleation of SA-Pt. Specifically, a high-concentration, large-sized nano-Pt with a dimension of ~10 nm can be observed on SWCNTs, which indicates that SWCNTs cannot provide suitable nucleation sites for SA-Pt (Figure 3a). This is in contrast to the very small amount of nano-Pt that is visible on the same scale on VG (Figure 3b). As shown in the HRSTEM image in Figure 2a for the same sample, SA-Pt is prevalent together with nano-Pt of very small dimensions in ALD Pt @VG. In fact, the dimension (~10 nm) of nano-Pt in the SWCNT case is significantly larger than that $(\sim 2-3 \text{ nm})$ in the VG case, as shown in the inset of Figure 3b. This indicates that the surface states of SWCNTs and VG are considerably different. One major difference is the presence of the edge states in VG, as shown in Figure 1. In addition, different growth approaches are employed to grow the SWCNTs (CVD) and VG (PECVD) samples. The plasma

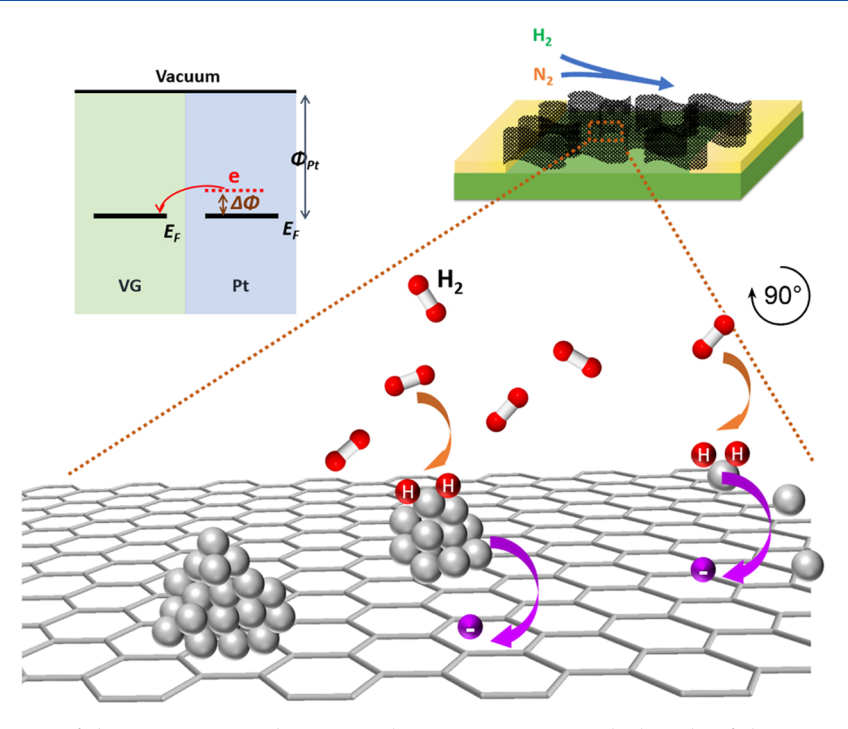


Figure 4. Schematic illustration of the H_2 -sensing mechanism on the Pt @VG sensor with the role of the Pt catalyst in the adsorption and decomposition of H_2 molecules, followed by a charge transfer process. Inset (left): schematic diagram showing charge transfer after H is adsorbed on Pt. E_F represents the Fermi energy level and Φ_{Pt} represents the work function of Pt. Inset (right): schematic illustration of Pt-decorated VG grown on SiO₂/Si substrates used for H_2 sensing.

in PECVD for VG growth, similar to the vertically aligned carbon nanofibers grown in a similar PECVD process, 42,43 introduces energetic ions around the growing carbon nanostructures, or specifically VG in this case, which promotes the growth of carbon nanostructures by decomposing the precursor and activating the sample surface. 42-46 Meanwhile, the bombardment of energetic ions on the growing carbon nanostructures is expected to promote the formation of dangling carbon bonds or defects on VG. In contrast, such dangling carbon bonds are almost absent in the SWCNTs grown using the thermal CVD process. Therefore, the lack of nucleation sites and more efficient Pt diffusion on the SWCNT wall would lead to the formation of larger-sized Pt NPs, as shown schematically in Figure 3c. In contrast, the presence of edge states and dangling carbon bonds on the wall of VG, which is supported by the higher I_D/I_G ratio of the VG sample than that of the SWCNTs in Figure 1d, would enable SA-Pt nucleation and hinder Pt diffusion, resulting in the formation of SA-Pt and a smaller sized nano-Pt on VG, as depicted schematically in Figure 3d.

As mentioned earlier, Pt precursor chemisorption and atom attachment preferentially occur at the defect sites on VG. During the first ALD cycle, all Pt atoms are assumed to be in the form of SA-Pt attached to the defect sites. In follow-up ALD cycles, three scenarios may occur. In the first scenario, precursor chemisorption can occur at defect sites not occupied during the first ALD cycle, followed by a reaction with O₂, resulting in the attachment of SA-Pt to VG. In the second scenario, precursor chemisorption may occur on the Pt atoms formed from the prior ALD cycle(s), leading to Ostwald ripening. In the third scenario, precursor chemisorption may occur on SA-Pt formed from the prior ALD cycle(s), but the Pt atoms or nano-Pt generated during the latter ALD cycle(s) may gain enough energy to migrate to nearby defect sites. The

first and third scenarios are more likely to occur, making SA-Pt dominant under lower ALD cycles, while nano-Pt becomes dominant at higher ALD cycles, as the availability of defect sites decreases and migration prevails. However, a second scenario can also occur, which is supported by the appearance of a small amount of nano-Pt at low ALD cycles (20 cycles). At a sufficiently high number of ALD cycles, at which the defect sites on VG are fully occupied, the second scenario of single Pt atoms growing into nano-Pt becomes predominant, resulting in a reduced percentage of single atoms. After 80 cycles, single atoms eventually disappeared completely.

DFT simulations further support this hypothesis, particularly regarding the formation of SA-Pt and nano-Pt. It was found that SA-Pt adsorption on SWCNT and HG with minimal defects was unstable, with Pt atoms consistently moving away from the surface. On the other hand, nano-Pt can stabilize on both the SWCNT and graphene basal planes. The calculated adsorption energy values of nano-Pt on SWCNT and graphene are -3.64 and -3.23 eV, respectively. These results suggest that Pt prefers to remain as nano-Pt on the SWCNT and HG, on which the dangling bonds are minimal (Figure 3c), while SA-Pt adsorption is unlikely. In a recent study, the adsorption of a single Pt atom at the edges of VG was investigated, 47 where it was demonstrated that SA-Pt can indeed be stabilized at the edges of VG with the assistance of O atoms that are present in proximity (Figure 3d). Similarly, Pt atoms tend to form stable bonds with CNT through two interfacial O atoms. 48 However, due to the minimal defect sites (where the C-O bond exists) on SWCNTs, the majority of SA-Pts lack energetic stability and tend to diffuse and cluster to the Pt atoms binding to the C-O bond near a defect site. This surface diffusion process subsequently initiates the nucleation of nano-Pt on the surface of the SWCNT. On the contrary, the dangling bonds on the edges of VG are abundant, which can

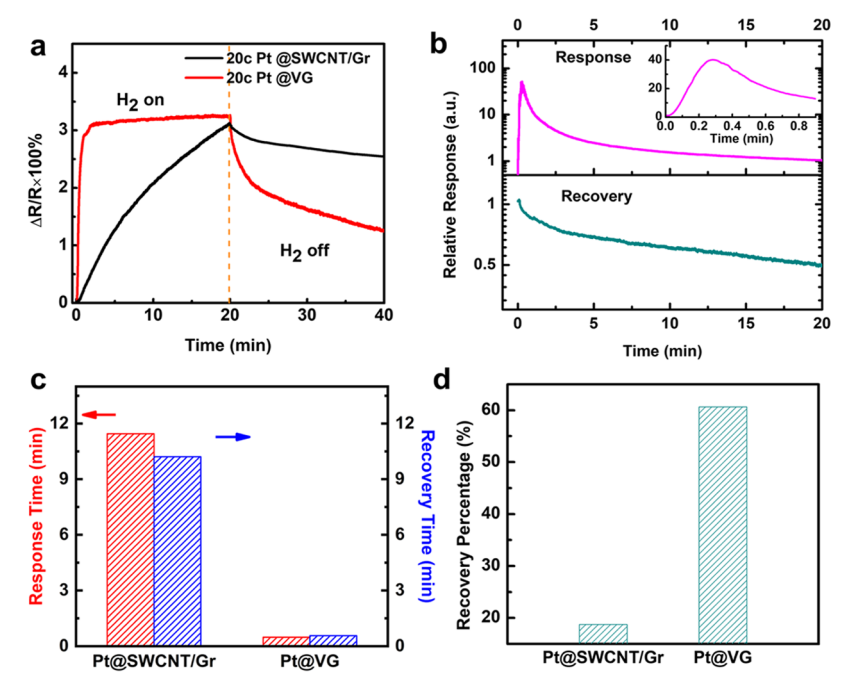


Figure 5. Comparison of the Pt @SWCNT/graphene nanohybrid (black) and Pt @VG (red) to 10% H_2 ; both samples have 20 c ALD Pt: (a) dynamic response; (b) relative response of Pt @VG with respect to the Pt @SWCNT/graphene nanohybrid replotted from (a); (c) response (0–70%) and recovery times (100–30%); and (d) recovery percentage after 20 min.

capture individual Pt atoms during the ALD Pt process to form SA-Pt, as shown in "Process 1" in Figure 3d may proceed in parallel to that similar to the SWCNT case on the sidewall of the VG, resulting in a similar diffusion and clustering process of Pt atoms and formation of nano-Pt as labeled "Process 2" in Figure 3d. However, the higher concentration of defects on the VG walls generated by plasma would reduce Pt diffusion, resulting in a smaller size of the nano-Pt formed.

It should be noted that the ALD growth of Pt does not introduce substantial changes or damage to the VG templates, as shown in the Raman spectra of the Pt @VG samples with 0, 20, 40, 60, and 80 c ALD cycles of Pt deposition (Figure S3a). Quantitatively, the $I_{\rm 2D}/I_{\rm G}$ ratios (red) of these five samples are comparable (Figure S3b). A similar trend can be seen in the $I_{\rm D}/I_{\rm G}$ ratio (black symbols in Figure S3b) of these samples, as exhibited by minimal changes in the ratios within the range of 0.02–0.17 for all samples. This suggests that the crystalline quality of the VG layers is not affected by the ALD Pt deposition, which is important for applications.

A practical application of Pt @ VG is the enhancement of H₂ sensing. H₂ sensing is crucial for ensuring safety in various applications, such as the automotive, industrial, and energy sectors, as it can detect leaks and measure hydrogen concentrations to prevent explosions and increase fuel cell efficiency. A gas sensor relies on the effective adsorption of gas molecules and charge transfer to the sensor. Although carbonbased materials have been used for sensing various gases, their performance in hydrogen sensing is typically poor due to their large activation energy, which results in inadequate adsorption of H₂ molecules. The decoration of a carbon-based gas sensor with Pt has been demonstrated to be an effective method for improving its sensing response to H₂. Pt not only adsorbs H₂ molecules but also facilitates the breaking and separation of H₂ molecules into H atoms at the outer surface of the Pt layers, a process known as dissociative chemisorption. As illustrated in Figure 4, H atoms readily dissolve in the Pt layer, thereby

lowering its work function. This leads to the transfer of electrons from the Pt layer to VG, consequently lowering its resistance (which is p-type under ambient conditions), thereby enhancing the response to H₂, as illustrated in the inset of Figure 4. To evaluate the catalytic properties of SA-Pt and nano-Pt, H₂ sensors based on VG with decorated ALD Pt were investigated, and the results are compared with SWCNT/ graphene nanohybrid counterparts, which were studied previously.⁴⁹

Figure 5a compares the dynamic response measured for 10% H₂ of 20 c ALD Pt @VG (red) and Pt @SWCNT/graphene nanohybrid (black). One striking difference between the two types of sensors is the significantly higher response speed of the Pt @VG sensor to both H2 turned on and off. Since SA-Pt dominates in the 20 c ALD Pt @VG sample, while large-sized nano-Pt dominates in the Pt @SWCNT/graphene nanohybrid, the faster speed could be ascribed to the much higher catalytic efficacy of SA-Pt. This also leads to a higher H₂ sensitivity. To quantify this, Figure 5b shows the responsivity $(\Delta R/R_0)$ of SA-Pt @VG normalized to that of its Pt @SWCNT/graphene nanohybrid counterparts as a function of time after H2 was turned on (top) and off (bottom). In the former (which reflects the enhancement factor of the response to H_2), the enhancement factor versus the time curve exhibits an inverted bell shape. It increases rapidly and reaches the peak enhancement factor of ~40 at ~0.3 min after H₂ is on. The enhancement factor started decreasing but remained above 1. Even at 20 min, the responsivity of the former is \sim 6.71% higher. After H₂ is turned off, the relative response exhibits a monotonic decreasing trend, i.e., the recovery speed of Pt @ VG is superior to that of the Pt @SWCNT/graphene nanohybrid. Figure 5c compares the response time (0-70% of the response process) and recovery time (100-30% of the recovery process) of Pt @VG and Pt @SWCNT/graphene hybrids. The former has a response time and recovery time of 0.48 and 1.57 min, about 23 and 7 times faster than the latter,

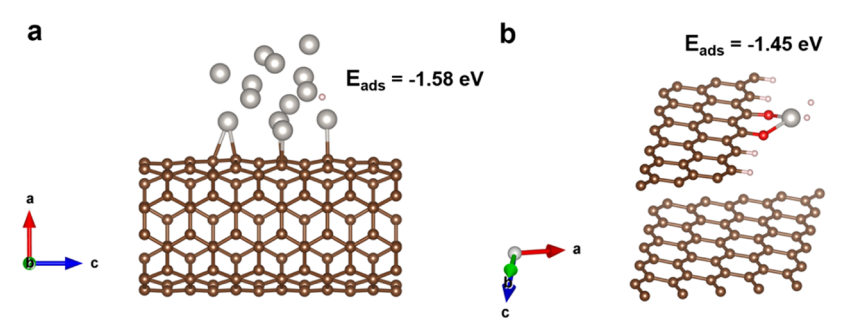


Figure 6. DFT optimized structures of hydrogen adsorption on (a) initial stage of nano-Pt formation on SWCNT, and (b) on Pt single-atom sites formed at the edges of VG.

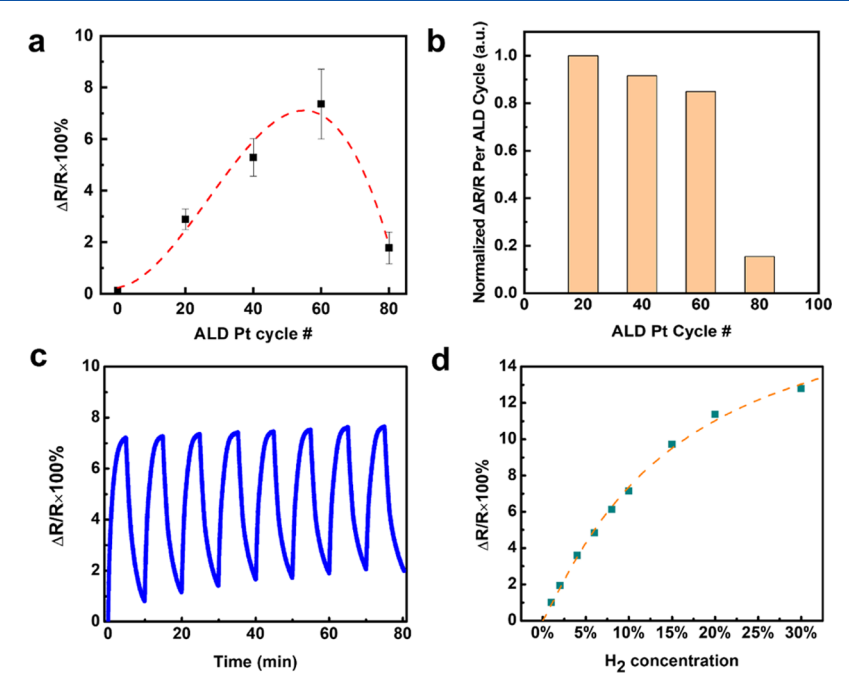


Figure 7. (a) Response of Pt @VG to 10% H_2 as a function of the number of ALD cycles. 0 c is the reference VG sample without ALD Pt. (b) Normalized response per ALD cycle to 10% H_2 as a function of the number of ALD cycles. (c) Dynamic response of the 60 c Pt @VG H_2 sensor measured with 10% H_2 alternating on/off. (d) Response of 60 c Pt @VG as a function of H_2 concentration. The orange dashed line is the fitting of the H_2 concentration dependence of the response in the form of the Langmuir adsorption model.

which has a response time and recovery time of 11.45 and 10.21 min, respectively.

The much faster response and recovery observed on Pt @ VG than on the Pt @SWCNT/graphene nanohybrid reflects the higher adsorption and desorption rate of H_2 on the SA-Pt @VG platform during H_2 sensing. According to Langmuir's theory of adsorption, 50 the adsorption rate ($R_{\rm ads}$) of gas molecules on metal can be expressed as 51,52

$$R_{\rm ads} = \frac{f(\theta)P}{\sqrt{2\pi mkT}} e^{-E_{\rm a}^{\rm ads}/RT} \tag{2}$$

where P is the gas pressure, m is the mass of the gas molecules, k is the Boltzmann constant, T is the temperature, and R is the gas constant. E_a^{ads} is the activation energy (barrier) for adsorption. $f(\theta)$ is a function proportional to $(1 - \theta)$, where θ represents the fraction of sites occupied by the adsorbent (i.e., the Langmuir definition of surface coverage). Based on this, the higher adsorption rate observed on SA-Pt can be attributed to two major reasons. One is the high effective surface area for the reaction since the SA-Pt dispersion on VG provides a high surface area for gas adsorption, unlike Pt nanoparticles on the

SWCNT/graphene nanohybrid, which has a smaller surface area than an equivalent amount of Pt. The increased surface area allows more H_2 molecules to interact with the Pt atoms on the graphene surface, resulting in a faster and more sensitive response. Another reason could be that the activation energy $E_{\rm a}^{\rm ads}$ for H_2 adsorption was lower on SA-Pt, which may be due to their isolated active sites and enhanced reactivity that facilitates the adsorption of H_2 molecules.

Similarly, the desorption rate (R_{des}) of gas molecules can be determined as follows

$$R_{\rm des} = \nu N^x e^{-E_{\rm a}^{\rm des}/RT} \tag{3}$$

where N is the surface concentration of the adsorbed species, x is the kinetic order of desorption, and $E_{\rm a}^{\rm des}$ is the activation energy (barrier) of desorption. ν is the frequency of vibration of the bond between the molecule and substrate, which can be understood as the frequency of attempts to break the bond and, hence, desorption. The higher desorption rate observed for SA-Pt @VG can be explained in two ways. On the one hand, due to the limited surface area of each single SA-Pt, as the number of chemisorbed H atoms increases, their bonding

with Pt is also affected by the electrostatic repulsion between H atoms, 33 resulting in more frequent attempts to break the H–Pt bonds (i.e., higher ν in eq 3). On the other hand, SA-Pt can also potentially lower the activation energy E_a^{des} for hydrogen desorption. A DFT study was conducted to examine the hydrogen adsorption energy E_{ads} on nano-Pt formed on SWCNT and on SA-Pt sites formed at the edges of VG. The theoretical models for these two structures are depicted in Figure 6a,6b, respectively. It was found that nano-Pt on SWCNT led to an H adsorption energy $E_{ads} = -1.58$ eV, while Pt single-atom sites on VG provided a relatively smaller H adsorption energy ($E_{ads} = -1.45$ eV). Since E_a^{ads} and E_a^{des} generally follow the relationship $E_a^{\text{des}} = E_a^{\text{ads}} - E_{\text{ads}}$ (considering $E_{\rm ads}$ is a negative value), smaller $E_{\rm a}^{\rm ads}$ and $E_{\rm ads}$ for SA-Pt @VG leads to smaller E_a^{des} , which is consistent with this speculation. Therefore, by combining these two factors, SA-Pt on VG facilitates the hydrogen desorption process, leading to faster recovery in Pt @VG. It is worth mentioning that the nanoparticles in Figure 4 are illustrated as Pt atoms stacked together, resembling the Pt nanoparticles formed on SWCNT. In contrast, the image in Figure 6 represents the initial stage of Pt atoms attached to the edges of vertical graphene during the ALD Pt deposition process, which is why some Pt atoms are not visually connected.

It should be noted that the calculated recovery time could not reflect the huge difference in recovery speed between these two samples since both devices did not show complete recovery after 20 min. Therefore, the recovery percentage, i.e., the level at which the resistance returned after reaching the peak value, is calculated and plotted for different substrates in Figure 5d. The resistance recovery of the Pt @VG sample is 61%, which is much higher than that of its SWCNT/graphene nanohybrid counterpart, which is only 19%.

The response to H₂ of Pt @VG with different ALD Pt cycles was also examined. Figure 7a depicts the maximum response of the Pt @VG sensor to 10% H₂ as a function of the number of ALD Pt cycles, which is adopted from Figure S4a which compares one cycle response of the Pt @VG sensors with 20 c (red), 40 c (blue), 60 c (green), and 80 c (purple) Pt. In addition, a reference sample with no ALD Pt deposition (black) is also included in Figure S4a, which exhibits a negligible H₂ response. The error bars in Figure 7a reflect sample-to-sample consistency since multiple samples (at least three) were measured for each Pt @VG device with the same number of ALD Pt cycles. The much higher H2 responsivity of Pt @VG devices demonstrates the significant role of the catalyst coated with Pt. Specifically, the amplitude of responsivity increases monotonically with the number of ALD Pt cycles up to 60 c. A peak responsivity of 9.41% was achieved for the sample with 60 c ALD Pt, which was ~90 times higher than that without the Pt catalyst. Interestingly, with a further increased number of ALD Pt cycles to 80 c or higher, the H₂ responsivity of Pt @VG decreases considerably, indicating the compromise of the relevant factors, including exposed Pt and carbon surfaces, since both may decrease as the nano-Pt size increases and Pt coverage of the VG surface. This trend is consistent with the observations on the Pt @SWCNT/ graphene nanohybrid in our previous report, 49 and could be explained as a trade-off between the two aspects of Pt coated on carbon nanostructures. The chemisorption of H2 molecules on Pt is the major contributor to the enhanced H2 sensing of the Pt @VG H₂ sensor. Hence, the denser the Pt particles on VG, the more H_2 chemisorption occurs.

As discussed previously, all samples with different ALD cycles of ALD Pt contain a mixture of SA-Pt and nano-Pt; both contribute to the catalytic effect in H₂ sensing. To evaluate their contributions quantitatively, the H₂ response exhibited in Figure 7a is replotted by normalizing it to the number of ALD cycles, assuming that the amount of Pt deposited in each ALD cycle is comparable. The normalized H₂ response to 10% H₂ is shown in Figure 7b. Interestingly, the 20 c sample has the highest value, which may be attributed to the higher catalytic effect of SA-Pt since it accounts for 83.1% of the total Pt (Figure S2). As the number of ALD cycles increases, the percentage of SA-Pt decreases, similar to the normalized H₂ response. This indicates that SA-Pt indeed makes a greater contribution to the H₂ response enhancement. On the other hand, if the ALD cycle number is increased above a certain threshold, the increased nano-Pt size and density will eventually lead to the merging of Pt nanostructures into a continuous Pt film coated on top of VG or SWCNT, which may block the H2 sensing area of the VG sensor, lowering the H_2 sensitivity. In order to examine the repeatability of Pt @VG H₂ sensors, dynamic response measurements were performed with respect to the pulses of H₂ at a 10% concentration. The response of the 60 c Pt @VG to 8 cycles of 10% H2 gas on/off was recorded and is exhibited in Figure 7c, demonstrating that repeatable behaviors were achieved on the Pt @VG H₂ sensors.

Figure S4b compares the response (0-70%) and recovery time (100–30%) of the Pt @VG responses to 10% H_2 at 20, 40, 60, and 80 c. All samples exhibit a very fast response and recovery within 2 min. However, no monotonic increasing or decreasing trend was observed as the number of ALD Pt cycles increased. Instead, the response time increases from 0.48 min at 20 c to 1.09 min at 40 c, slightly decreases to 1.07 min at 60 c, and eventually returns to 0.50 min at 80 °C. Interestingly, the recovery time variation shows an opposite trend, decreasing from 1.57 min at 20 c to 0.79 min at 40 c, further decreasing to 0.74 min at 60 c, and then increasing again to 1.49 min at 80 c. Currently, there is no clear explanation for this observation. However, for the Pt @VG samples, the response and recovery times are determined by the hydrogen adsorption/desorption rates. These rates are affected by both the morphology (SA-Pt contributes more to faster response/ recovery than nano-Pt) and the load (coverage) of SA-Pt deposited on VG. However, the TEM images demonstrated that both of these factors vary with increasing ALD cycle numbers from 20 to 80 c. The tangling of these two factors complicates the quantitative explanation of the variation in the response and recovery times among VG samples with different Pt ALD cycles.

The response of the Pt @VG $\rm H_2$ sensor to different $\rm H_2$ concentrations was also investigated. Figure 7d (adopted from Figure S5) depicts the response as a function of $\rm H_2$ concentration, showing a monotonically increasing trend over $\rm H_2$ concentrations ranging from 1 to 30%. This behavior is attributed to the higher quantity of $\rm H_2$ molecules absorbed on the surface of the Pt @VG sensors, resulting in a more pronounced alteration in the initial resistance. The $\rm H_2$ concentration dependence of the response $\Delta R/R_0$ could be fitted (orange dashed line in Figure 7d) in the form of the Langmuir adsorption model 54

$$\theta \propto \frac{K_c P_{\rm A}}{1 + K_c P_{\rm A}} \tag{4}$$

Table 1. Comparison of H₂-Sensing Performance with Earlier Reports on Pt-Decorated Carbon-Based H₂ Sensors

sensor materials	temperature (°C)	H_2 concentration	responsivity	specific responsivity	response time (min)	recovery time (min)	refs
Pt film/HG	175	1%	~4%	4	>5	N/A	58
nano-Pt/HG	65	1%	3.5%	3.5	N/A	N/A	59
nano-Pt/1L HG	200	1%	3.9%	3.9	0.2	0.4	60
nano-Pt/rGO	50	0.5%	8%	16	1	1.73	61
nano-Pt/vertical CNT	150	1%	1.1%	1.1	>10	>10	62
nano-Pt/MWCNT	RT	4%	6.5%	1.625	N/A	N/A	63
nano-Pt/MWCNT	RT	4%	17%	4.25	>20	>20	64
nano-Pt/MWCNT	RT	4%	8%	4	7	N/A	65
SA-Pt/VG	RT	1%	1.06%	1.06	1.07	0.74	this work

^aSpecific responsivity is calculated by dividing H₂ responsivity by H₂ concentration.

This describes the coverage of adsorbates θ in relation to their concentration (partial pressure $P_{\rm A}$) at adsorption equilibrium, where $K_{\rm c}$ is a constant. A higher coverage of adsorbed hydrogen will result in more charge transfer, thereby increasing the relative resistance change. Overall, within the H_2 concentration range of 1–30%, the experimental data agree well with the theory, as expected. It should be noted that the best sensitivity of 1% reported in this work is primarily the instrument limit of the current setup used for H_2 sensor characterization, considering that the safety threshold for H_2 is 4%. The actual detection limit of Pt @VG for hydrogen was > 1% with instrument modification.

Table 1 compares the H₂-sensing performance of SA-Pt @ VG with representative Pt-decorated carbon-based H₂ sensors. The SA-Pt @VG sample exhibits a responsivity comparable to that reported by others for Pt-decorated carbon-based materials measured at room temperature but demonstrates a significantly improved response speed (response time reduced to ~ 1 min compared to several of tens of minutes). The application of heat during H2-sensing measurements has been shown to enhance both the response and recovery speeds, as demonstrated in previous studies 55,56 (Table 1). This is not surprising considering that higher temperatures lead to increased rates of adsorption and desorption, as illustrated in eqs 2 and 3. This outcome demonstrates the feasibility of the SA-Pt catalyst as another approach to provide a rapid H₂ response without requiring heat. It should be noted that SA-Pt @VG is fairly stable when stored under ambient conditions. Figure S7 shows the sensitivity and stability results obtained for the SA-Pt @VG H2 sensor with 60 c Pt. The sensor retained 91% of its H₂ sensitivity after 11 days of storage under ambient conditions. Longer storage periods under ambient conditions typically result in further degradation of sensitivity. It is well known that the sensitivity of gas sensors based on carbon nanostructures degrades when stored under ambient conditions for an extended period, as the adsorption of molecules from the air accumulates on the surface of carbon nanostructures, hindering the adsorption of target gas molecules (H₂ in this case) during measurements. Interestingly, Alamri et al. reported that Pt NP-decorated SWCNT H₂ sensors⁵⁷ can be reactivated with restored sensitivity after storage under ambient conditions for extended periods.

4. CONCLUSIONS

In summary, this work reports a new approach for the synthesis of SA-Pt catalysts on VGs, which are potential 3D electrodes for the development of various sensors. Specifically, ALD was used to deposit Pt on VG taking advantage of the self-limiting effect for atomic-scale control of the Pt nominal thickness and

conformal coating over surfaces with a large aspect ratio. In addition, the edge states of VG were found to be critical for the stabilization of SA-Pt, as predicted by DFT simulations. The morphology of the Pt catalyst was studied as a function of the number of ALD cycles in the range of 0-80. SA-Pt and nano-Pt catalysts were found to coexist within this range, while the former was predominant at lower ALD cycles. With increasing the number of ALD cycles, the proportion of nano-Pt increased monotonically, including Pt clusters (<2 nm) and Pt NPs (>2 nm), and became dominant at higher ALD cycles in the range of 60-80. This result illustrates the importance of atomic-scale control of catalyst deposition and nucleation on the template to achieve SACs. However, SA-Pt and nano-Pt catalysts both provide substantial catalytic effects, and distinctive differences in catalytic efficiency and speed were observed in H2 sensing. Quantitatively, the response time of SA-Pt @VG H2 sensors can be more than an order of magnitude shorter than that of nano-Pt @VG or other carbon nanostructures decorated with a nano-Pt catalyst. The higher catalytic efficiency of SA-Pt is illustrated by the higher H₂ sensitivity of the SA-Pt @VG H2 sensors by more than an order of magnitude compared to their counterparts based on nano-Pt on various carbon nanostructures. This result illustrates the importance of atomic-scale control of the Pt catalyst formation, and the approach of combining ALD and VG is promising for achieving SA-Pt or other SACs for a variety of applications that benefit from high-efficiency and low-cost catalysts.

ASSOCIATED CONTENT

Solution Supporting Information

The Supporting Information is available free of charge at https://pubs.acs.org/doi/10.1021/acsanm.4c03416.

Additional experimental data; schematic showing the fabrication of ALD Pt @VG; cross-sectional SEM image of VG; histogram of Pt size distribution on VG; Raman spectra of VG with different ALD Pt cycles; single cycle on/off response to 10% H₂; H₂ on/off response of 60 c Pt @VG at different H₂ concentrations; LEIS data; and stability test (PDF)

AUTHOR INFORMATION

Corresponding Authors

Bo Liu – Department of Physics and Astronomy, The University of Kansas, Lawrence, Kansas 66045, United States; orcid.org/0000-0003-0298-8238; Email: liubo@ku.edu

Judy Z. Wu — Department of Physics and Astronomy, The University of Kansas, Lawrence, Kansas 66045, United States; Email: jwu@ku.edu

Authors

- Zhaojun Han CSIRO Manufacturing, Lindfield 2070 NSW, Australia; School of Chemical Engineering, The University of New South Wales, Kensington 2052 NSW, Australia; School of Mechanical, Medical and Process Engineering, Queensland University of Technology, Brisbane 4000 QLD, Australia; orcid.org/0000-0002-2437-319X
- Avi Bendavid CSIRO Manufacturing, Lindfield 2070 NSW, Australia; School of Materials Science and Engineering, The University of New South Wales, Kensington 2052 NSW, Australia; orcid.org/0000-0002-2454-9714
- Philip J. Martin CSIRO Manufacturing, Lindfield 2070 NSW, Australia
- Priyank V. Kumar School of Chemical Engineering, The University of New South Wales, Kensington 2052 NSW, Australia; Occid.org/0000-0002-8203-7223
- Yousof Haghshenas School of Chemical Engineering, The University of New South Wales, Kensington 2052 NSW, Australia
- Mohammed Alamri Department of Physics and Astronomy, The University of Kansas, Lawrence, Kansas 66045, United States; Department of Physics, Faculty of Science, Umm Al-Qura University, Makkah 21955, Saudi Arabia; orcid.org/0000-0002-7473-8644

Complete contact information is available at: https://pubs.acs.org/10.1021/acsanm.4c03416

Notes

The authors declare no competing financial interest.

■ ACKNOWLEDGMENTS

The authors acknowledge support in part by the US Army grant W909MY-21-C-0033, and US NSF grantd NSF-ECCS-2314401 and NSF-ECCS 2412220. Z.H. acknowledges the Future Fellowship (FT220100209) from the Australian Research Council.

REFERENCES

- (1) Kohl, D. The Role of Noble Metals in the Chemistry of Solid-State Gas Sensors. Sens. Actuators, B 1990, 1 (1-6), 158-165.
- (2) Miller, D. R.; Akbar, S. A.; Morris, P. A. Nanoscale Metal Oxide-Based Heterojunctions for Gas Sensing: A Review. *Sens. Actuators, B* **2014**, 204, 250–272.
- (3) Wu, G.; Zelenay, P. Nanostructured Nonprecious Metal Catalysts for Oxygen Reduction Reaction. *Acc. Chem. Res.* **2013**, 46 (8), 1878–1889.
- (4) Aslam, U.; Rao, V. G.; Chavez, S.; Linic, S. Catalytic Conversion of Solar to Chemical Energy on Plasmonic Metal Nanostructures. *Nat. Catal.* **2018**, *1* (9), 656–665.
- (5) Kohl, D. Function and Applications of Gas Sensors. J. Phys. D: Appl. Phys. 2001, 34 (19), R125-R149.
- (6) Alamri, M.; Liu, B.; Berrie, C. L.; Walsh, M.; Wu, J. Z. Probing the Role of CNTs in Pt Nanoparticle/CNT/Graphene Nanohybrids H2 Sensors. *Nano Express* **2022**, 3 (3), No. 035004.
- (7) Xiao, Z.; Kong, L. B.; Ruan, S.; Li, X.; Yu, S.; Li, X.; Jiang, Y.; Yao, Z.; Ye, S.; Wang, C.; Zhang, T.; Zhou, K.; Li, S. Recent Development in Nanocarbon Materials for Gas Sensor Applications. Sens. Actuators, B 2018, 274, 235–267.
- (8) Varghese, S.; Varghese, S.; Swaminathan, S.; Singh, K.; Mittal, V. Two-Dimensional Materials for Sensing: Graphene and Beyond. *Electronics* **2015**, 4 (3), 651–687.

- (9) Lin, Y. M.; Avouris, P. Strong Suppression of Electrical Noise in Bilayer Graphene Nanodevices. *Nano Lett.* **2008**, *8* (8), 2119–2125.
- (10) Novoselov, K. S.; Geim, A. K.; Morozov, S. V.; Jiang, D.; Zhang, Y.; Dubonos, S. V.; Grigorieva, I. V.; Firsov, A. A. Electric Field Effect in Atomically Thin Carbon Films. *Science* **2004**, *306* (5696), 666–669.
- (11) Tanaka, T.; Sano, E. Low-Frequency Noise in Carbon Nanotube Network Thin-Film Transistors. *Jpn. J. Appl. Phys.* **2014**, 53 (9), No. 090302.
- (12) Islam, A. Variability and Reliability of Single-Walled Carbon Nanotube Field Effect Transistors. *Electronics* **2013**, 2 (4), 332–367.
- (13) Liu, B.; Alamri, M.; Walsh, M.; Doolin, J. L.; Berrie, C. L.; Wu, J. Z. Development of an ALD-Pt@SWCNT/Graphene 3D Nanohybrid Architecture for Hydrogen Sensing. *ACS Appl. Mater. Interfaces* **2020**, *12* (47), 53115–53124.
- (14) Zheng, W.; Zhao, X.; Fu, W. Review of Vertical Graphene and Its Applications. ACS Appl. Mater. Interfaces 2021, 13 (8), 9561–9579
- (15) Bo, Z.; Mao, S.; Han, Z. J.; Cen, K.; Chen, J.; Ostrikov, K. K. Emerging Energy and Environmental Applications of Vertically-Oriented Graphenes. *Chem. Soc. Rev.* **2015**, *44* (8), 2108–2121.
- (16) Liu, L.; Corma, A. Metal Catalysts for Heterogeneous Catalysis: From Single Atoms to Nanoclusters and Nanoparticles. *Chem. Rev.* **2018**, *118* (10), 4981–5079.
- (17) Li, Z.; Tian, E.; Wang, S.; Ye, M.; Li, S.; Wang, Z.; Ma, Z.; Jiang, G.; Tang, C.; Liu, K.; Jiang, J. Single-Atom Catalysts: Promotors of Highly Sensitive and Selective Sensors. *Chem. Soc. Rev.* 2023, 52 (15), 5088–5134.
- (18) Chu, T.; Rong, C.; Zhou, L.; Mao, X.; Zhang, B.; Xuan, F. Progress and Perspectives of Single-Atom Catalysts for Gas Sensing. *Adv. Mater.* **2023**, 35 (3), No. e2206783.
- (19) He, H.; Wang, H. H.; Liu, J.; Liu, X.; Li, W.; Wang, Y. Research Progress and Application of Single-Atom Catalysts: A Review. *Molecules* **2021**, 26 (21), 6501.
- (20) Zeng, J.; Rong, Q.; Xiao, B.; Yu, R.; Zi, B.; Kuang, X.; Deng, X.; Ma, Y.; Zhang, J.; Wu, J.; Liu, Q. Single-Atom Silver Loaded on Tungsten Oxide with Oxygen Vacancies for High Performance Triethylamine Gas Sensors. *J. Mater. Chem. A* **2021**, *9* (13), 8704–8710.
- (21) Tian, R.; Ji, P.; Luo, Z.; Li, J.; Sun, J. Room-Temperature NH3 Gas Sensor Based on Atomically Dispersed Co with a Simple Structure. *New J. Chem.* **2021**, 45 (23), 10240–10247.
- (22) Malek, G. A.; Brown, E.; Klankowski, S. A.; Liu, J.; Elliot, A. J.; Lu, R.; Li, J.; Wu, J. Atomic Layer Deposition of Al-Doped ZnO/Al₂O₃ Double Layers on Vertically Aligned Carbon Nanofiber Arrays. *ACS Appl. Mater. Interfaces* **2014**, *6* (9), 6865–6871.
- (23) Vervuurt, R. H. J.; Kessels, W. M. M. E.; Bol, A. A. Atomic Layer Deposition for Graphene Device Integration. *Adv. Mater. Interfaces* **2017**, *4* (18), No. 1700232.
- (24) Kim, K.; Lee, H. B.; Johnson, R. W.; Tanskanen, J. T.; Liu, N.; Kim, M. G.; Pang, C.; Ahn, C.; Bent, S. F.; Bao, Z. Selective Metal Deposition at Graphene Line Defects by Atomic Layer Deposition. *Nat. Commun.* **2014**, *5*, No. 4781.
- (25) Tsounis, C.; Subhash, B.; Kumar, P. V.; Bedford, N. M.; Zhao, Y.; Shenoy, J.; Ma, Z.; Zhang, D.; Toe, C. Y.; Cheong, S.; Tilley, R. D.; Lu, X.; Dai, L.; Han, Z.; Amal, R. Pt Single Atom Electrocatalysts at Graphene Edges for Efficient Alkaline Hydrogen Evolution. *Adv. Funct. Mater.* 2022, 32 (38), No. 2203067.
- (26) Wang, X.; Jin, B.; Jin, Y.; Wu, T.; Ma, L.; Liang, X. Supported Single Fe Atoms Prepared Via Atomic Layer Deposition for Catalytic Reactions. ACS Appl. Nano Mater. 2020, 3 (3), 2867–2874.
- (27) Cheng, N.; Sun, X. Single Atom Catalyst by Atomic Layer Deposition Technique. *Chin. J. Catal.* **2017**, *38* (9), 1508–1514.
- (28) Fonseca, J.; Lu, J. Single-Atom Catalysts Designed and Prepared by the Atomic Layer Deposition Technique. ACS Catal. 2021, 11 (12), 7018–7059.
- (29) Han, Z. J.; Pineda, S.; Murdock, A. T.; Seo, D. H.; Ostrikov, K.; Bendavid, A. RuO₂-Coated Vertical Graphene Hybrid Electrodes for

- High-Performance Solid-State Supercapacitors. J. Mater. Chem. A 2017, 5 (33), 17293–17301.
- (30) Zhang, D.; Tsounis, C.; Ma, Z.; Djaidiguna, D.; Bedford, N. M.; Thomsen, L.; Lu, X.; Chu, D.; Amal, R.; Han, Z. Highly Selective Metal-Free Electrochemical Production of Hydrogen Peroxide on Functionalized Vertical Graphene Edges. *Small* **2022**, *18* (1), No. e2105082.
- (31) Aaltonen, T.; Ritala, M.; Sajavaara, T.; Keinonen, J.; Leskelä, M. Atomic Layer Deposition of Platinum Thin Films. *Chem. Mater.* **2003**, 15 (9), 1924–1928.
- (32) Kresse, G.; Furthmuller, J. Efficient Iterative Schemes for Ab Initio Total-Energy Calculations Using a Plane-Wave Basis Set. *Phys. Rev. B* **1996**, *54* (16), 11169–11186.
- (33) Kresse, G.; Hafner, J. Ab Initio Molecular-Dynamics Simulation of the Liquid-Metal-Amorphous-Semiconductor Transition in Germanium. *Phys. Rev. B* **1994**, *49* (20), 14251–14269.
- (34) Kresse, G.; Joubert, D. From Ultrasoft Pseudopotentials to the Projector Augmented-Wave Method. *Phys. Rev. B* **1999**, *59* (3), 1758.
- (35) Perdew, J. P.; Burke, K.; Ernzerhof, M. Generalized Gradient Approximation Made Simple. *Phys. Rev. Lett.* **1996**, 77 (18), 3865.
- (36) Larsen, A. H.; Mortensen, J. J.; Blomqvist, J.; Castelli, I. E.; Christensen, R.; Dułak, M.; Friis, J.; Groves, M. N.; Hammer, B.; Hargus, C. The Atomic Simulation Environment a Python Library for Working with Atoms. *J. Phys.: Condens.Matter* **2017**, 29 (27), No. 273002.
- (37) Gong, M.; Liu, Q.; Cook, B.; Kattel, B.; Wang, T.; Chan, W. L.; Ewing, D.; Casper, M.; Stramel, A.; Wu, J. Z. All-Printable ZnO Quantum Dots/Graphene Van Der Waals Heterostructures for Ultrasensitive Detection of Ultraviolet Light. *ACS Nano* **2017**, *11* (4), 4114–4123.
- (38) Ferrari, A. C.; Meyer, J. C.; Scardaci, V.; Casiraghi, C.; Lazzeri, M.; Mauri, F.; Piscanec, S.; Jiang, D.; Novoselov, K. S.; Roth, S.; Geim, A. K. Raman Spectrum of Graphene and Graphene Layers. *Phys. Rev. Lett.* **2006**, *97* (18), No. 187401.
- (39) Pal, A. N.; Ghosh, A. Ultralow Noise Field-Effect Transistor from Multilayer Graphene. *Appl. Phys. Lett.* **2009**, 95 (8), No. 082105.
- (40) Ni, Z.; Wang, Y.; Yu, T.; Shen, Z. Raman Spectroscopy and Imaging of Graphene. *Nano Res.* **2008**, *1* (4), 273–291.
- (41) Dresselhaus, M. S.; Dresselhaus, G.; Saito, R.; Jorio, A. Raman Spectroscopy of Carbon Nanotubes. *Phys. Rep.* **2005**, *409* (2), 47–99.
- (42) Klankowski, S. A.; Pandey, G. P.; Malek, G.; Thomas, C. R.; Bernasek, S. L.; Wu, J.; Li, J. Higher-Power Supercapacitor Electrodes Based on Mesoporous Manganese Oxide Coating on Vertically Aligned Carbon Nanofibers. *Nanoscale* **2015**, *7* (18), 8485–8494.
- (43) Malek, G. A.; Brown, E.; Klankowski, S. A.; Liu, J.; Elliot, A. J.; Lu, R.; Li, J.; Wu, J. Atomic Layer Deposition of Al-Doped ZnO/Al₂O₃ Double Layers on Vertically Aligned Carbon Nanofiber Arrays. *ACS Appl. Mater. Interfaces* **2014**, *6* (9), 6865–6871.
- (44) Bo, Z.; Yang, Y.; Chen, J.; Yu, K.; Yan, J.; Cen, K. Plasma-Enhanced Chemical Vapor Deposition Synthesis of Vertically Oriented Graphene Nanosheets. *Nanoscale* **2013**, *5* (12), 5180–5204.
- (45) Yang, C.; Bi, H.; Wan, D.; Huang, F.; Xie, X.; Jiang, M. Direct Pecvd Growth of Vertically Erected Graphene Walls on Dielectric Substrates as Excellent Multifunctional Electrodes. *J. Mater. Chem. A* **2013**, *1* (3), 770–775.
- (46) Sun, J.; Rattanasawatesun, T.; Tang, P.; Bi, Z.; Pandit, S.; Lam, L.; Wasen, C.; Erlandsson, M.; Bokarewa, M.; Dong, J.; Ding, F.; Xiong, F.; Mijakovic, I. Insights into the Mechanism for Vertical Graphene Growth by Plasma-Enhanced Chemical Vapor Deposition. ACS Appl. Mater. Interfaces 2022, 14 (5), 7152–7160.
- (47) Tsounis, C.; Subhash, B.; Kumar, P. V.; Bedford, N. M.; Zhao, Y.; Shenoy, J.; Ma, Z.; Zhang, D.; Toe, C. Y.; Cheong, S.; Tilley, R. D.; Lu, X.; Dai, L.; Han, Z.; Amal, R. Pt Single Atom Electrocatalysts at Graphene Edges for Efficient Alkaline Hydrogen Evolution. *Adv. Funct. Mater.* **2022**, 32 (38), 2203067 DOI: 10.1002/adfm.202203067.
- (48) Yan, H.; Lin, Y.; Wu, H.; Zhang, W.; Sun, Z.; Cheng, H.; Liu, W.; Wang, C.; Li, J.; Huang, X.; Yao, T.; Yang, J.; Wei, S.; Lu, J.

- Bottom-up Precise Synthesis of Stable Platinum Dimers on Graphene. *Nat. Commun.* **2017**, 8 (1), No. 1070.
- (49) Liu, B.; Alamri, M.; Walsh, M.; Doolin, J. L.; Berrie, C. L.; Wu, J. Z. Development of an Ald-Pt@Swcnt/Graphene 3d Nanohybrid Architecture for Hydrogen Sensing. ACS Appl. Mater. Interfaces 2020, 12 (47), 53115–53124.
- (50) Langmuir, I. The Constitution and Fundamental Properties of Solids and Liquids. Part I. Solids. *J. Am. Chem. Soc.* **1916**, 38 (11), 2221–2295.
- (51) Brancher, R. D.; Stefanov, S.; Graur, I.; Frezzotti, A. A Kinetic Model for Gas Adsorption-Desorption at Solid Surfaces under Non-Equilibrium Conditions. *Vacuum* **2020**, *174*, No. 109166.
- (\$2) Butt, H.-J.; Graf, K.; Kappl, M. Physics and Chemistry of Interfaces, 4th ed.; Wiley-VCH, 2023; pp 219-230.
- (53) Cheng, N.; Stambula, S.; Wang, D.; Banis, M. N.; Liu, J.; Riese, A.; Xiao, B.; Li, R.; Sham, T. K.; Liu, L. M.; Botton, G. A.; Sun, X. Platinum Single-Atom and Cluster Catalysis of the Hydrogen Evolution Reaction. *Nat. Commun.* **2016**, *7*, No. 13638.
- (54) Patiha; Heraldy, E.; Hidayat, Y.; Firdaus, M. The Langmuir Isotherm Adsorption Equation: The Monolayer Approach. *IOP Conf. Ser.: Mater. Sci. Eng.* **2016**, *107*, No. 012067.
- (55) Ha, N. H.; Long, C. T.; Nam, N. H.; Hue, N. T.; Phuong, N. H.; Hong, H. S. Characteristics of Hydrogen Sensor Based on Monolayer of Pt Nanoparticles Decorated on Single-Layer Graphene. *J. Electron. Mater.* **2017**, *46* (6), 3353–3358.
- (56) Lu, X.; Song, X.; Gu, C.; Ren, H.; Sun, Y.; Huang, J. Freeze Drying-Assisted Synthesis of Pt@Reduced Graphene Oxide Nanocomposites as Excellent Hydrogen Sensor. *J. Phys. Chem. Solids* **2018**, 116, 324–330.
- (57) Alamri, M. A.; Liu, B.; Walsh, M.; Doolin, J. L.; Berrie, C. L.; Wu, J. Z. Enhanced H₂ Sensitivity in Ultraviolet-Activated Pt Nanoparticle/SWCNT/Graphene Nanohybrids. *IEEE Sens. J.* **2021**, 21 (18), 19762–19770.
- (58) Chu, B. H.; Lo, C. F.; Nicolosi, J.; Chang, C. Y.; Chen, V.; Strupinski, W.; Pearton, S. J.; Ren, F. Hydrogen Detection Using Platinum Coated Graphene Grown on Sic. Sens. Actuators, B 2011, 157 (2), 500–503.
- (59) Zhu, L.; Jia, Y.; Gai, G.; Ji, X.; Luo, J.; Yao, Y. Ambipolarity of Large-Area Pt-Functionalized Graphene Observed in H2 Sensing. Sens. Actuators, B 2014, 190, 134–140.
- (60) Ha, N. H.; Long, C. T.; Nam, N. H.; Hue, N. T.; Phuong, N. H.; Hong, H. S. Characteristics of Hydrogen Sensor Based on Monolayer of Pt Nanoparticles Decorated on Single-Layer Graphene. *J. Electron. Mater.* **2017**, 46 (6), 3353–3358.
- (61) Lu, X.; Song, X.; Gu, C.; Ren, H.; Sun, Y.; Huang, J. Freeze Drying-Assisted Synthesis of Pt@Reduced Graphene Oxide Nanocomposites as Excellent Hydrogen Sensor. *J. Phys. Chem. Solids* **2018**, 116, 324–330.
- (62) Penza, M.; Rossi, R.; Alvisi, M.; Signore, M. A.; Cassano, G.; Dimaio, D.; Pentassuglia, R.; Piscopiello, E.; Serra, E.; Falconieri, M. Characterization of Metal-Modified and Vertically-Aligned Carbon Nanotube Films for Functionally Enhanced Gas Sensor Applications. *Thin Solid Films* **2009**, *517* (22), *6211–6216*.
- (63) Kumar, M. K.; Ramaprabhu, S. Nanostructured Pt Functionlized Multiwalled Carbon Nanotube Based Hydrogen Sensor. *J. Phys. Chem. B* **2006**, *110* (23), 11291–11298.
- (64) Kaniyoor, A.; Ramaprabhu, S. Hybrid Carbon Nanostructured Ensembles as Chemiresistive Hydrogen Gas Sensors. *Carbon* **2011**, *49* (1), 227–236.
- (65) Kaniyoor, A.; Imran Jafri, R.; Arockiadoss, T.; Ramaprabhu, S. Nanostructured Pt Decorated Graphene and Multi Walled Carbon Nanotube Based Room Temperature Hydrogen Gas Sensor. *Nanoscale* **2009**, *1* (3), 382–386.